# On Stochastic Reduction in Laser-Assisted Dielectric Breakdown for Programmable Nanopore Fabrication

Zifan Tang, † Ming Dong, † Xiaodong He, † and Weihua Guan †, ‡\*

<sup>&</sup>lt;sup>†</sup> Department of Electrical Engineering, Pennsylvania State University, University Park, Pennsylvania 16802, United States

<sup>&</sup>lt;sup>‡</sup> Department of Biomedical Engineering, Pennsylvania State University, University Park, Pennsylvania 16802, United States

<sup>\*</sup> Corresponding Author, Email: w.guan@psu.edu, Tel: 1-814-867-5748

### **ABSTRACT**

The controlled dielectric breakdown emerged as a promising alternative towards accessible solidstate nanopore fabrication. Several prior studies have shown laser-assisted dielectric breakdown could help control the nanopore position and reduce the possibility of forming multiple pores. Here we developed a physical model to estimate the probability of forming a single nanopore under different combinations of the laser power and the electric field. This model relies on the materialand experiment-specific parameters: the Weibull statistical parameters and the laser-induced photothermal etching rate. Both the model and our experimental data suggest that a combination of a high laser power and a low electric field is statistically favorable for forming a single nanopore at a programmed location. While this model relies on experiment-specific parameters, we anticipate it could provide the experimental insights for nanopore fabrication by laser-assisted dielectric breakdown method, enabling broader access to solid-state nanopores and their sensing applications.

# **KEYWORDS**

Solid-state nanopore, laser-assisted dielectric breakdown, stochastic reduction, single nanopore, single molecule detection

### INTRODUCTION

Solid-state nanopores offer promising label-free detection of single molecules such as DNAs<sup>1-6</sup>, RNAs<sup>7-8</sup>, proteins<sup>9-10</sup>, and DNA-protein complexes<sup>11-12</sup>. Conventional solid-state nanopore fabrication methods involve focused electron beams<sup>13</sup> or ion beams<sup>14-15</sup> for physical bombardment. However, due to limited throughput and high complexity, nanopore-based sensing has limited accessibility for ordinary labs. An alternative controlled breakdown (CBD) method for nanopore fabrication was demonstrated to tackle these challenges<sup>16-20</sup>, relying on the electric field-induced physical breakdown of the dielectric material. Nevertheless, the stochastic nature of the breakdown makes it challenging to predetermine the number and location of the nanoscale pinhole<sup>16, 21-25</sup>. A single nanopore is desirable for most single-molecule experiments. Besides, many nanopore-based applications such as tunneling current sensing<sup>26-27</sup> and plasmonic nanopores<sup>28-33</sup> would require the nanopore to be localized specifically around an existing structure. So far, CBD-based nanopore localization efforts were predominately made by focusing the electric field through using tip-based technology<sup>34-35</sup>, selectively thinning the membrane<sup>36</sup>, or fabricating pyramid structures on the membrane<sup>37</sup>. These methods often require additional apparatus or lithography patterning processes, thus limiting their flexibility and tunability.

Several recent studies have demonstrated that a focused laser beam can be used for nanopore fabrication in SiN<sub>x</sub> membranes. This can be simply performed in the air without an additional electric field or in the electrolyte solutions with an external electric field for the dielectric breakdown. For example, Yuan *et al.* showed that directly drilling the SiN<sub>x</sub> membrane in the air can fabricate sub 100 nm nanopore by applying Watt-level nanosecond laser pulses<sup>38</sup>. Ying *et al.* demonstrated that infrared laser-assisted controlled breakdown could significantly reduce the probability of forming multiple nanopores<sup>39</sup>. Gilboa *et al.* showed that a focused laser beam with mW-intensity could irreversibly etch SiN<sub>x</sub> membranes in 1 M KCl, resulting in nanopores formation. They also found that the etching process was susceptible to the relative content of Si over N atoms in the SiN<sub>x</sub> membrane<sup>40</sup>. Yamazaki *et al.* showed that the SiN<sub>x</sub> etching rate was influenced by the supporting electrolyte and suggested the photothermal effect was responsible for the SiN<sub>x</sub> dissolution process<sup>41</sup>. These prior studies, while different in their laser specifications, electric field strength, unambiguously suggested laser-assisted CBD could help control the nanopore position and reduce the possibility of forming multiple pores.

In this work, we investigated the impact of the surrounding environment, the electric field, and the laser power on the probability of forming a single nanopore at the focused laser spot, with the aim to optimize the laser-assisted dielectric breakdown. We developed a physical model to project the confidence level of creating a single nanopore at different combinations of laser power and electric field. The model relies on material-specific properties (Weibull statistical parameters) and experimental-specific parameters (laser-induced photothermal etching rate). With the guidance of this model, we experimentally probed the nanopore number and location using the ionic current enhancement method<sup>42-43</sup>. Both the model and experimental results suggested that a high laser power and a low electric field is a favorable combination for creating a single nanopore at the focused laser spot. Our findings would provide insights into optimizing the laser-assisted dielectric breakdown towards solid-state nanopore fabrication and localization.

# **RESULTS AND DISCUSSION**

# Principle of Laser-Assisted Dielectric Breakdown

The dielectric breakdown under the influence of a biasing electric field is a well-studied phenomenon. A nanoscale pinhole could be created in the membrane when the density of accumulated defects reaches a critical value<sup>16</sup>. However, defect generation is a random process<sup>22-24</sup>, which leads to poor control over the location of nanopore formation (**Figure 1a**). Multiple pores can be formed due to the stochastic subsequent nanopore creation between the occurrence of the first breakdown and the time when the applied voltage is terminated. Several works have demonstrated the laser-assisted dielectric breakdown for solid-state nanopore localization<sup>39-41, 44</sup>. The laser-localized thinning down facilitates the electric field enhancement at the laser spot. Since the defect generation efficiency increases exponentially with the electric field, the laser spot would have a much higher probability of first reaching the breakdown critical trap density (**Figure 1b**).

**Figure 1c** shows the schematic of our custom-built nanopore fabrication and characterization setup. A 488 nm Gaussian-profile laser beam was focused onto the SiN<sub>x</sub> membrane assembled in an optically accessible flow cell. A CMOS camera was used to provide a bright-field view. A single photon counting module (SPCM) was used for photoluminescence (PL) characterization of the material. A pair of Ag/AgCl electrodes across the membrane was used to apply a voltage for

the dielectric breakdown. This setup enabled us to perform the laser-assisted dielectric breakdown, scanning PL for material characterization, and laser-enhanced ionic current mapping<sup>42-43</sup> for nanopore location in a single platform (see **Methods** for details of the setup).

# Kinetics of Laser-Induced Photothermal Etching of SiN<sub>x</sub> in Electrolyte

While the laser-induced thinning of  $SiN_x$  in the electrolyte solution was universally observed, the underlying mechanism is controversial<sup>40-41</sup>. To better understand the thinning kinetics in our experiments, we performed the laser radiation experiments on 30 nm-thick  $SiN_x$  membranes with a focused 488 nm laser both in the air and in the electrolyte solution.

In the air, we sequentially radiated a  $5\times4$  array at five different laser powers (4-20 mW) and varying exposure time (10-60 min). We then characterized this sample with scanning PL<sup>45</sup> and atomic force microscopy (AFM). **Figure 2a** shows the PL result. Evident PL reductions were observable at the laser exposed locations. However, the AFM characterization (**Figure 2b**) showed no visible thickness change at the laser spots. This existence of the PL change and the absence of thickness change suggests that the focused laser with power up to 20 mW only altered the microscopic electronic structures of the SiN<sub>x</sub> (photochemical effect) in the air<sup>45</sup>, rather than physical etching.

For the solution experiment, a 5×4 array was exposed in 2 M KCl with 10 mM Tris and 1 mM EDTA with the same laser dose as in the air. As shown in **Figure 2c** and **Figure 2d**, both the PL intensity and the AFM-obtained membrane thickness showed significant reductions in the laser-exposed area. This result suggested that the 20 mW laser not only altered the microscopic electronic structures <sup>45</sup> but also 'etched' the SiN<sub>x</sub> membrane in the 2 M KCl solution. To examine if the laser 'etching' of the SiN<sub>x</sub> in the electrolyte stems from the photothermal decomposition of the material, we performed a finite-element simulation to estimate the photothermal heating of the solution (**Figure S1**). We found the temperature (175°C) caused by the 20 mW laser is far below the SiN<sub>x</sub> decomposition temperature (1500 °C)<sup>41</sup>. As a result, the laser 'etching' of the SiN<sub>x</sub> in 2 M KCl in our experiment could not be ascribed to the photothermal decomposition of the material. In fact, the contrast of the experiments performed in the air and in the solution suggested that the laser-SiN<sub>x</sub> reactivity is a convoluted photochemical and photothermal process. The focused laser not only alters the microscopic electronic structures of the SiN<sub>x</sub> (photochemical effect), but also provides the heat for promoting the photothermal etching. It is no surprise that the surrounding

environment would play a significant role due to their different heat dissipation coefficient and chemical composition<sup>41</sup>.

To establish the relationship between the laser power and the etching rate in our experiment, we examined the AFM-obtained etching profile (**Figure S2**). The etching rate, defined by the maximal depth in the center of the etching profile, can be well fitted with the laser power to the Arrhenius equation<sup>46</sup>,

$$k = Ae^{-\frac{E_a}{R(bP+T_0)}} \tag{1}$$

where k is the etching rate (Å/min), A is the Arrhenius constant for the reaction (Å/min),  $E_a$  is the activation energy (kJ/mol), R is the gas constant, b is the photothermal coefficient (K/mW), P is the laser power (mW),  $T_0$  is the room temperature. Note that  $bP+T_0$  is the laser-induced temperature. The activation energy  $E_a$  fitted from **Figure 2e** was estimated to be 13.7 kJ/mol (see **Table S1** for Arrhenius fitting parameters). Note that these parameters are SiN<sub>x</sub> material-specific and experimental setup-specific and could vary from one lab to the other<sup>39-41</sup>. This excellent fitting to the Arrhenius equation suggests that the laser 'etching' of the SiN<sub>x</sub> membrane in the solution results from the chemical reaction between the aqueous electrolyte and SiN<sub>x</sub> membrane, promoted by the photothermal effect.

#### Confidence Model of Laser-Assisted Dielectric Breakdown

When an insulating membrane is continuously subjected to electric field stress, the number of traps in the membrane increases with time. Once the trap density reaches a critical value, the breakdown occurs<sup>22, 24</sup>. The time to breakdown is a stochastic process governed by the probability of forming a connected path across the membrane, following the Weibull distribution<sup>22, 24</sup>,

$$f(t) = \frac{\beta}{\lambda} \left(\frac{t}{\lambda}\right)^{\beta - 1} e^{(-(t/\lambda)^{\beta})} \tag{2}$$

where f(t) is the breakdown probability after the electric field is applied for a time t,  $\beta$  is the shape parameter which characterizes the steepness of the breakdown transition,  $\lambda$  is the characteristic lifetime at which 63% of membranes have experienced a breakdown. Note that the average breakdown time of a Weibull distribution can be derived from  $\lambda \Gamma (1 + 1/\beta)$ , which corresponds within  $\pm 10\%$  to  $\lambda$  for typical values of  $\beta$ . For simplicity, the characteristic lifetime  $\lambda$  was used to describe the average time to breakdown in the following context.

Two competing processes coincided with the typical laser-assisted dielectric breakdown setup. One is the normal breakdown, and the other is the laser-assisted breakdown (**Figure 1a** and **b**). The average time to breakdown in the areas with no laser can be estimated as 16, 22, 47,

$$\lambda_n = Be^{-\gamma E_n} \quad (3)$$

in which n stands for normal, B is integration constant (s), and the  $\gamma$  is the field acceleration factor (nm/V),  $E_n$  is the electric field.

At the laser spot, the electric field  $E_{la}(t)$ , will increase over time due to local etching of the SiN<sub>x</sub>. The breakdown efficiency (*i.e.*, percentage of failure created by unit time) is given by  $1/Be^{-\gamma E_{la}(t)}$ . If the same trap density is required for the breakdown to occur at the laser spot, one could estimate the average time to breakdown at the laser spot by (**Table S2**),

$$\int_0^{\lambda_{la}} \frac{dt}{Be^{-\gamma E_{la}(t)}} = \int_0^{\lambda_{la}} \frac{d_0 - kt}{d_0} dt \quad (4)$$

where la stands for laser-assisted, k is the laser power-dependent etching rate (Eq.1),  $d_0$  is the membrane thickness.

By estimating  $\lambda_n$  and  $\lambda_{la}$  using Eq.3 and Eq.4, the time to breakdown distributions for the normal breakdown  $f_n(t)$  and for the laser-assisted breakdown  $f_{la}(t)$  can be assessed by Eq. 2. However, note that Weibull statistical parameters ( $\beta$  and  $\lambda$ ) remain unknown and could vary from lab to lab due to material and setup differences. One has to estimate these Weibull parameters from existing experimental data. Using our experimentally derived parameters (Table S3), Figure 3a shows a representative  $f_n(t)$  and  $f_{la}(t)$  profile. Figure 3b shows the cumulative distribution function (CDF) of the time to breakdown time. The overlapping of  $f_n(t)$  and  $f_{la}(t)$  indicates the uncertainty of nanopore localization. The smaller the overlap, the higher the probability of nanopore localization will be. One can estimate the confidence for forming the nanopore at the laser spot by using,

$$C = 1 - \int_0^\infty \min(f_n(t), f_{la}(t)) dt \quad (5)$$

With this model, we can estimate the nanopore localization confidence under various combinations of laser power and electric field using our experiment-derived parameters. **Figure 3c** shows a representative example (parameters for this plot were listed in **Table S4**). We observed several interesting features. First, low laser power could not help achieve nanopore localization

due to the insignificant photothermal etching. The breakdown behavior in this region is equivalent to the normal CBD. Second, a high electric field always leads to random nanopore generation (confidence~0). This is because a high electric field can immediately break down the material at a random location, making the contribution of the laser-assisted etching irrelevant. Third, at a fixed low electric field, increasing the laser power could always enhance the confidence level. Note that the quantitative result in **Figure 3c** represents a specific case in our experiment and should not be generalized for other setups without knowing the material and experimental-specific parameters.

# **Probing Specific Cases in the Confidence Model**

Based on the confidence model, we experimentally probed the laser-assisted breakdown at different electric fields (0.5-1 V/nm) and laser powers (**Figure 3d**). We used our previously reported moving Z-score method for breakdown fabrication (flowchart shown in **Figure S3**)<sup>21</sup> and used the ionic current mapping method for nanopore location determination<sup>42-43</sup>.

Figure 3d (i-iii) shows the results from samples under 20 mW laser at different electric fields. The top microscope images show the laser spot location before the nanopore fabrication. The bottom ionic current scanning images show the nanopore location after the fabrication. At low electric field (0.5 V/nm) and intermediate electric field (0.8 V/nm), we observed a single ionic current enhancement in the laser spot. While the laser beam spatial resolution is insufficient to resolve if there are several nanopores within the laser focal spots, we believe it is unlikely to form multiple nanopores within the 1 µm laser focal spot because the center of the etched pit has the highest electric field and is the most likely location for the initial breakdown (Figure S2). Therefore, the single ionic current enhancement is a good indication of a single nanopore at 0.5 V/nm and 0.8 V/nm. However, at a high electric field (1 V/nm, Figure 3d (iii)), the ionic current mapping showed that formed pores were not in the laser spot and could be random in numbers. The resulting ionic current is also much larger (>100 nA). This uncontrolled nanopore generation at the high electric fields is consistent with model predictions. At high electric fields, relatively slow laser-assisted thinning can be easily overwhelmed by the fast electrical breakdown (Figure S4), rendering the benefits of laser irrelevant. We also tested different electric field conditions at a low laser power (5 mW, Figure 3d (iv-vi)). We observed the same trend that a high electric field can negatively impact the confidence of forming a single nanopore in the laser spot.

The behaviors of these representative cases and the normal breakdown fabrication result

(**Figure S5**) showed a good agreement with the model predictions in **Figure 3c**. Both the model and experiment results suggested that a combination of high laser power and a low electric field is preferred towards single nanopore localization. Admittedly, a full examination of the confidence model would require testing many more samples by different labs to establish sufficient statistics in the future.

#### **Programmable Nanopore Fabrication**

With the knowledge of the optimized conditions for single nanopore localization, we set out to test if the laser-assisted breakdown can be programmed to fabricate a single nanopore at an arbitrary spot. A total of 8 different samples were tested. We intentionally focused the laser spots at different places and varied the electric field from 0.03 V/nm to 0.4 V/nm (i.e., low electric field). The top row of Figure 4a shows the laser spot location on the SiN<sub>x</sub> membrane before the breakdown. The bottom row of Figure 4a shows the corresponding ionic current mapping for determining the location and number of the formed nanopores. We observed a single ionic current enhancement in each of these samples, indicating a single nanopore. The nanopore position matched the laser spot location very well (Figure 4b). These results suggested a low electric field at 20 mW laser in a very robust combination for forming single nanopores at the laser spot in our setup. We also studied the impact of the electric field on the nanopore formation time and the nanopore size. Note that the fabrication time follows the Weibull distribution at a specific electric field <sup>21</sup>. It would require a significant number of breakdown experiments to probe the statistics at each electric field, which is tedious and costly to perform. Instead, we performed a single sampling at each electric field condition and examined the general trend. Figure 4c shows the relationship between the electric field and fabrication time. In general, the fabrication time decreases with the increasing electric field. Figure 4d shows the relationship between the electric field and the nanopore size, which was estimated from the ionic conductance measurement (Figure S7). As shown in Figure 4d, the nanopore diameter tends to decrease with reducing the electric field. This is because less enlargement can occur after the initial breakdown event happened at low electric field<sup>21</sup>.

### **DNA Translocation Experiments**

To demonstrate the sensing performance of laser-assisted breakdown nanopores. We

performed single molecule translocation experiments using 100 pM 48.5 kbp double-stranded  $\lambda$ -DNA. **Figure 5a** shows a representative time-trace of current using a nanopore of 10 nm diameter (estimated by the conductance measurement). The initially stable open pore current (15.7 nA) was interrupted by current blockage events of 0.3-3 nA magnitude. The magnified insets in **Figure 5a** show typical translocation event. Dual current blockage levels were captured, which reflects that the  $\lambda$ -DNA molecules translocated with the folded structure. **Figure 5b** shows a scatter plot of current blockages versus dwell time for a total of 238 translocation events. The average dwell time was 53 ms, and the average blockage was 0.6 nA, comparable to previous studies<sup>41, 44</sup>.

To confirm the current drop indeed stems from the single molecule translocation through a single nanopore and verify the nanopore size, we examined the ratio of blocked pore current ( $i_b$ =15.1 nA) to the open pore current ( $i_0$ =15.7 nA) as  $i_b/i_0 = 1 - d_{DNA}^2/d^2$ , in which  $d_{DNA}$  and d are the diameter of DNA (2.2 nm) and the diameter of the nanopore, respectively<sup>48</sup>. The estimated nanopore diameter using the above method is about 11 nm, which is in excellent agreement with the diameter estimated by the IV measurement (10 nm). This agreement confirmed that a single nanopore was formed in the fabrication and the current drop indeed stems from the single molecule translocation. **Figure 5c** shows the power spectrum density (PSD) of the ionic current. The root-mean-square (RMS) noise at 10 kHz bandwidth was about 30 pA, sufficiently small for distinguishing typical single molecule events with dip magnitude >300 pA. It is noteworthy that the nanopores formed by the laser-assisted breakdown method exhibited a stable baseline current and reduced noise, comparing with nanopores fabricated by the normal breakdown (**Figure S8**). The exact mechanism behind the improved noise performance using laser-assisted breakdown fabrication warrants further exploration.

### CONCLUSION

In conclusion, we studied the laser-assisted dielectric breakdown for localizing a single nanopore at a programmed location with the aim of addressing the stochastic issue in the normal breakdown method. A statistic model was developed to estimate the confidence of nanopore localization at different laser powers and electric fields. We experimentally probed three representative regions of the confidence map, and the results were qualitatively consistent with model predictions. Future work will focus on gathering more experimental data to test this model. While the utility of this model is subject to parameter variations in membrane material properties,

laser wavelength, and electrolyte, we found that a combination of high laser power and low electric field was generally favorable for forming a single nanopore at the laser spot. The nanopore fabricated by laser-assisted dielectric breakdown exhibited excellent noise performances<sup>49</sup> for single-molecule translocation experiments. We believe this study provided significant experimental insights into optimizing the laser-assisted dielectric breakdown and would enable broader access to robust solid-state nanopore fabrication and sensing applications.

### **METHODS**

Materials and Chemicals. Low-stress SiN<sub>x</sub> membranes on 200 μm thick lightly doped silicon substrates were used in our experiments (Norcada, Canada). The SiN<sub>x</sub> membranes are 15 nm and 30 nm in thickness with a  $50\times50~\mu\text{m}^2$  window. Before mounting into our custom-built PMMA based flow cell, the SiN<sub>x</sub> membranes were cleaned in oxygen plasma for 120 s at 50 W to facilitate the wetting of the membrane surface. Ag/AgCl electrodes were house-made with 0.2-0.375 mm Ag wires (Warner Instruments, Hamden, USA). λ-DNA (48.5 kbp, 0.3 μg/μl) was purchased from ThermoFisher. PBS, KCl, and Tris-EDTA solution (pH 8.0) were purchased from Sigma-Aldrich. Ecoflex-5 used as an insulating sealant of the SiN<sub>x</sub> chip was obtained from Smooth-On, Inc. Prior to use, all solutions were filtered with a 0.2 μm Anotop filter (Whatman plc).

**Instrumentation.** The SiN<sub>x</sub> membrane chip was sealed onto a custom-built flow cell with a transparent quartz coverslip bottom, forming the *cis* and *trans* chambers. Both sides of the chambers were filled with KCl solution. Two Ag/AgCl electrodes were inserted into the KCl solution and electrically connected to a source meter unit (Keithley 2636) through a BNC cable. The chamber opposing the Si etch pit was grounded in our work unless otherwise stated. 488 nm (Coherent OBIS 488 LS) laser beams were focused onto a spatial pinhole (1-25+B-1+M-0.5, National Aperture) by an objective lens (M-5X, Newport) to reject out-of-focus light. The laser beams were re-collimated by an achromatic doublet (AC254-075-A, Thorlabs) and focused by an objective lens (RMS40X-PF, Thorlabs). The radius of the laser beam spot was 1 μm (FWHM, inset (ii) of **Figure 1c**). The flow cell was mounted onto a 3D manual positioner above the microscope objective. The emitted light was collected by the same objective and directed at a CMOS camera (DCC1545M, Thorlabs) by a dichroic mirror (BB2-E02, Thorlabs). The entire

assembly was shielded inside a Faraday cage to minimize electromagnetic interferences.

Photoluminescence Characterization. The PL characterization was obtained by a customized LabVIEW program (National Instruments) that controls the motion of the nanopositioner as well as collects the photon counting signals. The typical parameters for obtaining the scanned PL results in our experiments are 100 nm step size, 1 mW laser power, and 2 ms integration time. The counted emission photons were normalized to the integration time and the incident laser power (cpms/mW: counter per millisecond/ milliwatt).

**Atomic Force Microscopy Characterization.** AFM measurements were performed on a Dimension Icon (Bruker) AFM microscope using Peak Force tapping mode. A triangular-shaped ScanAsyst-Air tip was used in this study. During the measurement, the peak force set point was set to 2 nN. The scan was performed at a scan rate of 0.226 Hz and 512 lines per sample.

Nanopore Fabrication and Validation. The buffer used in the etching rate experiment was performed in 2M KCl with 10 mM Tris and 1 mM EDTA (pH 7.4). All the nanopores (both with and without laser-assisted) were fabricated by the moving Z-Score method with 1 M KCl with 10 mM Tris and 1mM EDTA. The flowchart of the automated procedure for moving Z-score can be found in our previous work<sup>21</sup>. The feedback time of the customized LabView program is 20 ms. The number and the location of nanopores were validated by ionic current mapping. The typical parameters used for ionic current mapping were 2-4 mW laser power, 100 mV voltage, and 10-20 μm/s scanning speed.

**DNA Sensing.** λ-DNA was added to the *cis* chamber to a final concentration of 100 pM. The Ag/AgCl electrodes were then connected to the Axopatch 200B amplifier (Molecular Devices, CA) with a 300 mV bias voltage. The amplified signal was filtered with a 4-pole Bessel set at 10 kHz and digitalized by a 16-bit/100 MHz DAQ card (NI 6363, Texas Instruments). Data analysis was carried out by using customized MATLAB code to extract the duration and depth of each current blockade events.

ASSOCIATED CONTENT

Supplementary Information is available.

Detailed descriptions of COMSOL simulation, AFM characterized etching profile, laser-assisted

nanopore fabrication, pore diameter characterization data, parameters for Arrhenius fitting, and

confidence model information (PDF).

**AUTHOR INFORMATION** 

**Corresponding Author** 

\* Email: w.guan@psu.edu

**ORCID** 

Weihua Guan: 0000-0002-8435-9672

**Author contributions** 

T.Z., D.M., and H.X. built the experimental setup. Z.T. carried out the fabrication and sensing

experiment and developed the statistical model. W.G. conceived the concept and supervised the

study. W.G. and T.Z. co-wrote the manuscript, discussed it with all other authors.

**NOTES** 

The authors declare no competing financial interest.

**ACKNOWLEDGMENTS** 

This work supported by the National Science Foundation under Grant No. 1710831, 1902503, and

1912410. Any opinions, findings, and conclusions or recommendations expressed in this work are

those of the authors and do not necessarily reflect the views of the National Science Foundation.

13

# FIGURES AND CAPTIONS

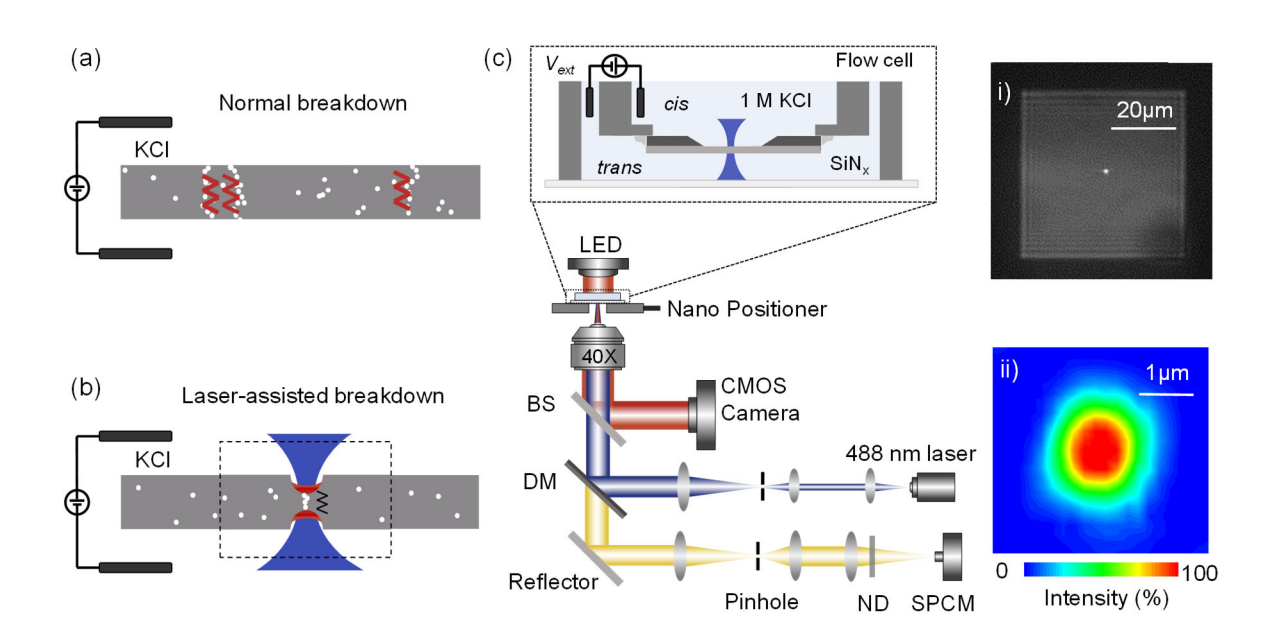


**Figure 1**. Schematic drawing of the nanopore fabrication by (a) normal breakdown and (b) laser-assisted breakdown. The drawings are for illustrative purposes and not to scale. (c) Schematic of the custom-built nanopore fabrication and characterization system. (BS: beam splitter, DM: dichroic mirror, ND: neutral-density filter). The focused laser spot at an arbitrary location on the membrane (inset i) and the Gaussian intensity profile of the laser (inset ii).

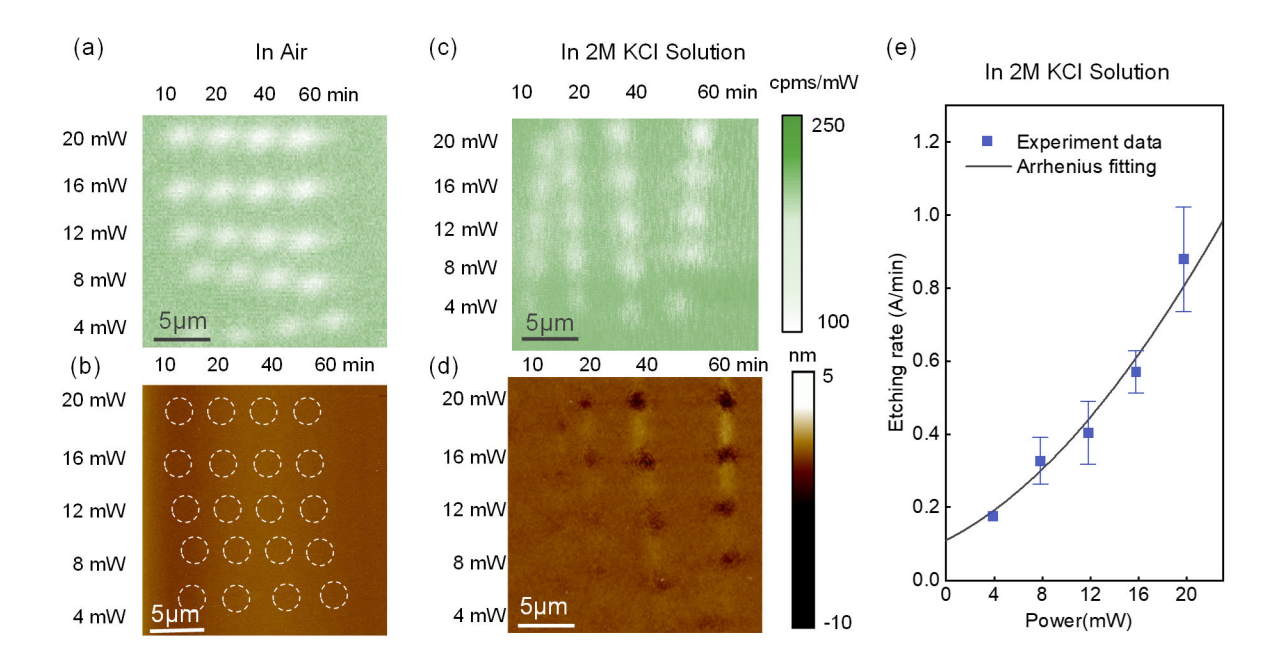


**Figure 2**. (a) Photoluminescence (PL) probed after exposing the  $SiN_x$  to the laser in the air. (b) AFM characterization of the sample exposed in the air (dash circles are the laser exposed regions). The counted emission photons were normalized to the integration time and the incident laser power (cpms/mW: counter per millisecond/milliwatt). No significant morphology change was observed. (c) PL probed after exposing the  $SiN_x$  to the laser in 2 M KCl solution. (d) AFM characterization of the sample exposed in 2 M KCl solution. The material etching was visible in the laser spots. (e) Extracted  $SiN_x$  etching rate as a function of the laser power. Note that the measured etching rate is the maximum etching rate in the membrane thickness direction. The solid line is the Arrhenius fitting. The PL map was obtained by scanning at 1 mW laser power with 200 nm step and 2 ms integration time.

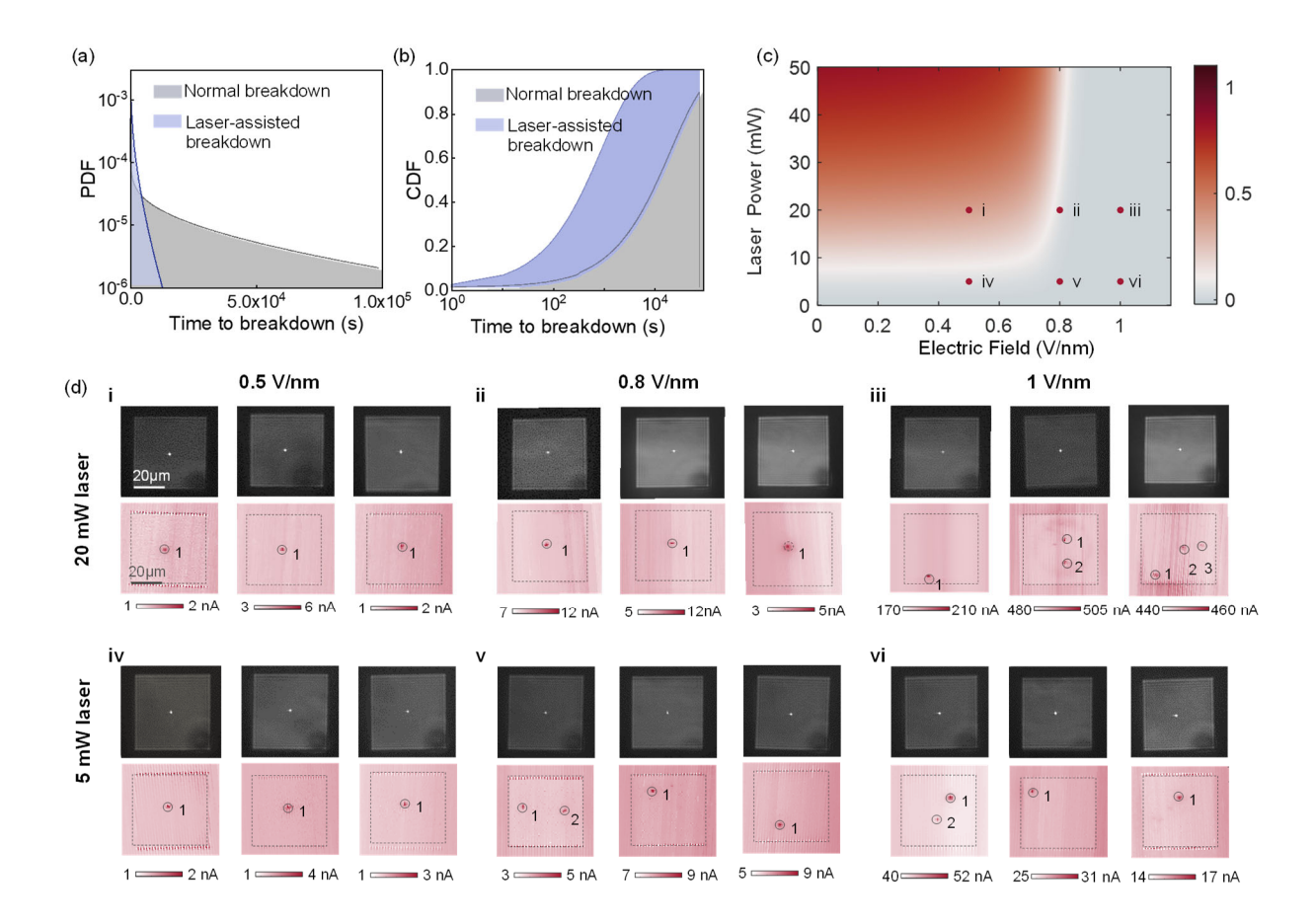


**Figure 3**. (a) PDF and (b) CDF of representative Weibull distribution of time to breakdown for the normal and laser-assisted breakdown. (Parameters: Normal breakdown: 0.6 V/nm; Laser-assisted breakdown: 0.6 V/nm and 50 mW laser;  $\lambda_n = 24501$ s,  $\lambda_{la} = 1362$ s,  $\beta = 0.63$ ). (c) Calculated confidence map of single nanopore localization at different laser powers and electric fields. Parameters used: integration constant  $B = 5 \times 10^{15}$  s, field acceleration factor  $\gamma = 38$  nm/V, membrane thickness  $d_0 = 30$  nm, photothermal coefficient b = 8.06 K/mW, shape parameter  $\beta = 0.63$ . (d) laser-assisted breakdown at different electric fields (0.5-1 V/nm) and laser powers (5 and 20 mW). The top panels are microscope images with bright spots showing the locations of the focused laser spot. The bottom panels are ionic current mapping results, performed at 4 mW laser power and 100 mV voltage with 10 μm/s scanning speed. The PDF and CFD of all cases can be found in Figure S6.

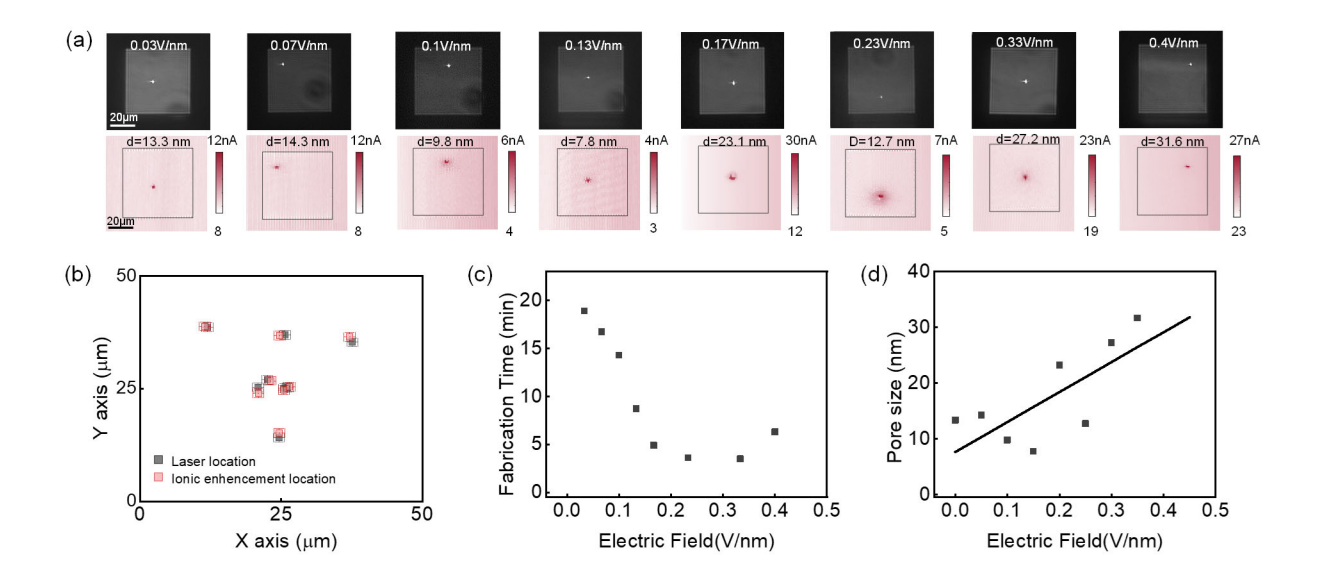


**Figure 4**. (a) Programmable laser-assisted breakdown fabrication using 20 mW laser and low electric field ranging from 0.03 V/nm to 0.4 V/nm. The bright spots in the top microscope images show the laser location. The bottom laser enhanced ionic current mappings show the number and location of the fabricated nanopores. All ionic current mapping experiments were performed at 2 mW laser power and 100 mV voltage with 20  $\mu$ m/s scanning speed. (b) Overlay of the extracted laser location and the formed nanopore location. The error bar indicates the full width at half maximum (FWHM). (c) The nanopore fabrication time as a function of the electric field. (d) The formed nanopore diameter as a function of the electric field. The nanopore diameter is determined by the IV measurement. The line in (d) is used to guide the eyes.

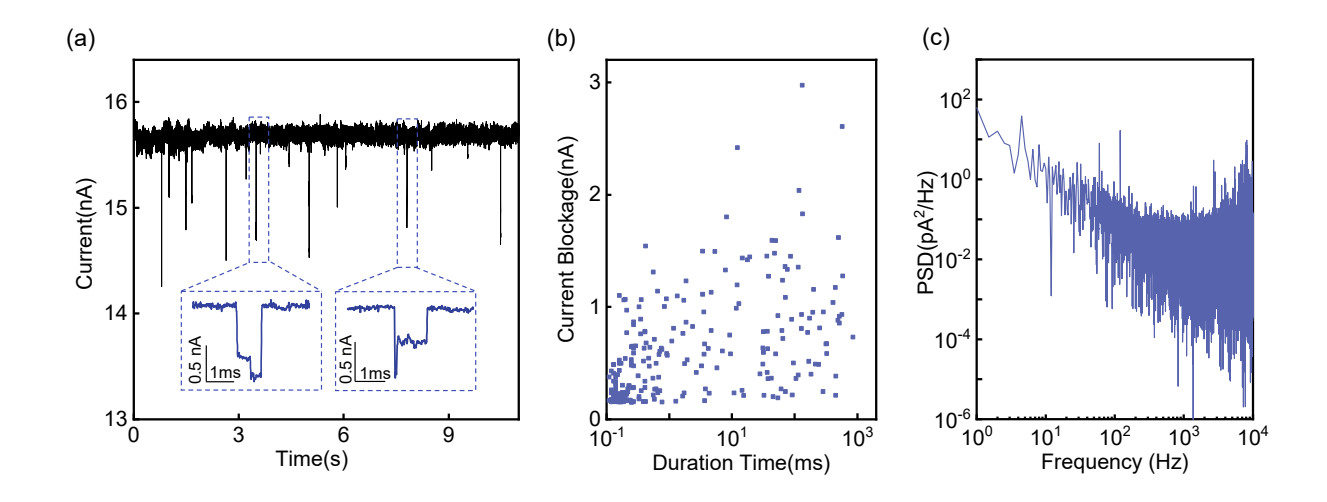


**Figure 5**. (a) A representative current time-trace for 100 pM 48.5 kbp  $\lambda$ -DNA molecules translocating through a 10 nm nanopore at 300 mV bias. The magnified insets show two typical ionic current blockades during the translocation. (b) Scatter plot of the current blockades versus dwell time for a total of 238 translocation events. (c) Power spectrum density (PSD) of the ionic current obtained at 300 mV with a low-pass filter at 10 kHz.

#### REFERENCES

- (1) Dekker, C. Solid-state nanopores. *Nature nanotechnology* **2007**, *2* (4), 209-215.
- (2) Storm, A. J.; Storm, C.; Chen, J.; Zandbergen, H.; Joanny, J.-F.; Dekker, C. Fast DNA translocation through a solid-state nanopore. *Nano letters* **2005**, *5* (7), 1193-1197.
- (3) Venkatesan, B. M.; Bashir, R. Nanopore sensors for nucleic acid analysis. *Nature nanotechnology* **2011**, *6* (10), 615-624.
- (4) Tang, Z.; Choi, G.; Nouri, R.; Guan, W. Loop-Mediated Isothermal Amplification-Coupled Glass Nanopore Counting Toward Sensitive and Specific Nucleic Acid Testing. *Nano letters* **2019**, *19* (11), 7927-7934.
- (5) Nouri, R.; Jiang, Y.; Lian, X. L.; Guan, W. Sequence-Specific Recognition of HIV-1 DNA with Solid-State CRISPR-Cas12a-Assisted Nanopores (SCAN). *ACS sensors* **2020**, *5* (5), 1273-1280.
- (6) Fologea, D.; Gershow, M.; Ledden, B.; McNabb, D. S.; Golovchenko, J. A.; Li, J. Detecting single stranded DNA with a solid state nanopore. *Nano letters* **2005**, *5* (10), 1905-1909.
- (7) Henley, R. Y.; Ashcroft, B. A.; Farrell, I.; Cooperman, B. S.; Lindsay, S. M.; Wanunu, M. Electrophoretic deformation of individual transfer RNA molecules reveals their identity. *Nano letters* **2016**, *16* (1), 138-144.
- (8) Skinner, G. M.; van den Hout, M.; Broekmans, O.; Dekker, C.; Dekker, N. H. Distinguishing single-and double-stranded nucleic acid molecules using solid-state nanopores. *Nano Letters* **2009**, *9* (8), 2953-2960.
- (9) Wilson, J.; Sloman, L.; He, Z.; Aksimentiev, A. Graphene nanopores for protein sequencing. *Advanced functional materials* **2016**, *26* (27), 4830-4838.
- (10) Yusko, E. C.; Johnson, J. M.; Majd, S.; Prangkio, P.; Rollings, R. C.; Li, J.; Yang, J.; Mayer, M. Controlling protein translocation through nanopores with bio-inspired fluid walls. *Nature nanotechnology* **2011**, *6* (4), 253-260.
- (11) Hornblower, B.; Coombs, A.; Whitaker, R. D.; Kolomeisky, A.; Picone, S. J.; Meller, A.; Akeson, M. Single-molecule analysis of DNA-protein complexes using nanopores. *Nature Methods* **2007**, *4* (4), 315-317.
- (12) Celaya, G. e.; Perales-Calvo, J.; Muga, A.; Moro, F.; Rodriguez-Larrea, D. Label-free, multiplexed, single-molecule analysis of protein–dna complexes with nanopores. *ACS nano* **2017**, *11* (6), 5815-5825.
- (13) Storm, A.; Chen, J.; Ling, X.; Zandbergen, H.; Dekker, C. Fabrication of solid-state nanopores with single-nanometre precision. *Nature materials* **2003**, *2* (8), 537-540.
- (14) Li, J.; Stein, D.; McMullan, C.; Branton, D.; Aziz, M. J.; Golovchenko, J. A. Ion-beam sculpting at nanometre length scales. *Nature* **2001**, *412* (6843), 166-169.
- (15) Lanyon, Y. H.; De Marzi, G.; Watson, Y. E.; Quinn, A. J.; Gleeson, J. P.; Redmond, G.; Arrigan, D. W. Fabrication of nanopore array electrodes by focused ion beam milling. *Analytical chemistry* **2007**, *79* (8), 3048-3055.
- (16) Kwok, H.; Briggs, K.; Tabard-Cossa, V. Nanopore fabrication by controlled dielectric breakdown. *PloS one* **2014**, *9*, e92880.
- (17) Briggs, K.; Kwok, H.; Tabard Cossa, V. Automated Fabrication of 2 nm Solid State Nanopores for Nucleic Acid Analysis. *Small* **2014**, *10* (10), 2077-2086.
- (18) Yanagi, I.; Akahori, R.; Hatano, T.; Takeda, K.-i. Fabricating nanopores with diameters of sub-1 nm to 3 nm using multilevel pulse-voltage injection. *Scientific reports* **2014**, *4*, 5000.
- (19) Yanagi, I.; Akahori, R.; Takeda, K.-i. Stable fabrication of a large nanopore by controlled

- dielectric breakdown in a high-pH solution for the detection of various-sized molecules. *Scientific reports* **2019**, *9*, 13143.
- (20) Waugh, M.; Briggs, K.; Gunn, D.; Gibeault, M.; King, S.; Ingram, Q.; Jimenez, A. M.; Berryman, S.; Lomovtsev, D.; Andrzejewski, L. Solid-state nanopore fabrication by automated controlled breakdown. *Nature Protocols* **2020**, *15* (1), 122-143.
- (21) Roshan, K. A.; Tang, Z.; Guan, W. High fidelity moving Z-score based controlled breakdown fabrication of solid-state nanopore. *Nanotechnology* **2019**, *30*, 095502.
- (22) Briggs, K.; Charron, M.; Kwok, H.; Le, T.; Chahal, S.; Bustamante, J.; Waugh, M.; Tabard-Cossa, V. Kinetics of nanopore fabrication during controlled breakdown of dielectric membranes in solution. *Nanotechnology* **2015**, *26*, 084004.
- (23) Dong, M.; Tang, Z.; He, X.; Guan, W. Direct Observation of Redox Induced Bubble Generation and Nanopore Formation Dynamics in Controlled Dielectric Breakdown. *ACS Applied Electronic Materials* **2020**, *2* (9), 2954-2960.
- (24) Lombardo, S.; Stathis, J. H.; Linder, B. P.; Pey, K. L.; Palumbo, F.; Tung, C. H. Dielectric breakdown mechanisms in gate oxides. *Journal of applied physics* **2005**, *98*, 121301.
- (25) Wang, Y.; Ying, C.; Zhou, W.; de Vreede, L.; Liu, Z.; Tian, J. Fabrication of multiple nanopores in a SiN x membrane via controlled breakdown. *Scientific reports* **2018**, *8*, 1234.
- (26) Ivanov, A. P.; Freedman, K. J.; Kim, M. J.; Albrecht, T.; Edel, J. B. High precision fabrication and positioning of nanoelectrodes in a nanopore. *ACS nano* **2014**, *8* (2), 1940-1948.
- (27) Krishnakumar, P.; Gyarfas, B.; Song, W.; Sen, S.; Zhang, P.; Krstic, P.; Lindsay, S. Slowing DNA translocation through a nanopore using a functionalized electrode. *ACS nano* **2013**, *7* (11), 10319-10326.
- (28) Nicoli, F.; Verschueren, D.; Klein, M.; Dekker, C.; Jonsson, M. P. DNA translocations through solid-state plasmonic nanopores. *Nano letters* **2014**, *14* (12), 6917-6925.
- (29) Crick, C. R.; Albella, P.; Ng, B.; Ivanov, A. P.; Roschuk, T.; Cecchini, M. P.; Bresme, F.; Maier, S. A.; Edel, J. B. Precise attoliter temperature control of nanopore sensors using a nanoplasmonic bullseye. *Nano letters* **2015**, *15* (1), 553-559.
- (30) Cecchini, M. P.; Wiener, A.; Turek, V. A.; Chon, H.; Lee, S.; Ivanov, A. P.; McComb, D. W.; Choo, J.; Albrecht, T.; Maier, S. A. Rapid ultrasensitive single particle surface-enhanced raman spectroscopy using metallic nanopores. *Nano letters* **2013**, *13* (10), 4602-4609.
- (31) Belkin, M.; Chao, S.-H.; Jonsson, M. P.; Dekker, C.; Aksimentiev, A. Plasmonic nanopores for trapping, controlling displacement, and sequencing of DNA. *ACS nano* **2015**, *9* (11), 10598-10611.
- (32) Jonsson, M. P.; Dekker, C. Plasmonic nanopore for electrical profiling of optical intensity landscapes. *Nano letters* **2013**, *13* (3), 1029-1033.
- (33) Pud, S.; Verschueren, D.; Vukovic, N.; Plesa, C.; Jonsson, M. P.; Dekker, C. Self-aligned plasmonic nanopores by optically controlled dielectric breakdown. *Nano letters* **2015**, *15* (10), 7112-7117.
- (34) Arcadia, C. E.; Reyes, C. C.; Rosenstein, J. K. In situ nanopore fabrication and single-molecule sensing with microscale liquid contacts. *ACS nano* **2017**, *11* (5), 4907-4915.
- (35) Zhang, Y.; Miyahara, Y.; Derriche, N.; Yang, W.; Yazda, K.; Capaldi, X.; Liu, Z.; Grutter, P.; Reisner, W. Nanopore Formation via Tip Controlled Local Breakdown Using an Atomic Force Microscope. *Small Methods* **2019**, *3*, 1900147.
- (36) Carlsen, A. T.; Briggs, K.; Hall, A. R.; Tabard-Cossa, V. Solid-state nanopore localization by controlled breakdown of selectively thinned membranes. *Nanotechnology* **2017**, *28*, 085304.
- (37) Wang, Y.; Chen, Q.; Deng, T.; Liu, Z. Nanopore fabricated in pyramidal HfO2 film by

- dielectric breakdown method. Applied Physics Letters 2017, 111, 143103.
- (38) Yuan, Y.; Li, G.; Zaribafzadeh, H.; de la Mata, M.; Castro-Hartmann, P.; Zhang, Q.; Arbiol, J.; Xiong, Q. Sub-20 nm nanopores sculptured by a single nanosecond laser pulse. *arXiv* **2018**, *1806*, 08172.
- (39) Ying, C.; Houghtaling, J.; Eggenberger, O. M.; Guha, A.; Nirmalraj, P.; Awasthi, S.; Tian, J.; Mayer, M. Formation of single nanopores with diameters of 20–50 nm in silicon nitride membranes using laser-assisted controlled breakdown. *ACS nano* **2018**, *12* (11), 11458-11470.
- (40) Gilboa, T.; Zvuloni, E.; Zrehen, A.; Squires, A. H.; Meller, A. Automated, Ultra Fast Laser Drilling of Nanometer Scale Pores and Nanopore Arrays in Aqueous Solutions. *Advanced Functional Materials* **2020**, *30*, 1900642.
- (41) Yamazaki, H.; Hu, R.; Zhao, Q.; Wanunu, M. Photothermally assisted thinning of silicon nitride membranes for ultrathin asymmetric nanopores. *ACS nano* **2018**, *12* (12), 12472-12481.
- (42) Di Fiori, N.; Squires, A.; Bar, D.; Gilboa, T.; Moustakas, T. D.; Meller, A. Optoelectronic control of surface charge and translocation dynamics in solid-state nanopores. *Nature nanotechnology* **2013**, *8* (12), 946-951.
- (43) Assad, O. N.; Di Fiori, N.; Squires, A. H.; Meller, A. Two color DNA barcode detection in photoluminescence suppressed silicon nitride nanopores. *Nano letters* **2015**, *15* (1), 745-752.
- (44) Gilboa, T.; Zrehen, A.; Girsault, A.; Meller, A. Optically-monitored nanopore fabrication using a focused laser beam. *Scientific reports* **2018**, *8*, 9765.
- (45) He, X.; Tang, Z.; Liang, S.; Liu, M.; Guan, W. Confocal scanning photoluminescence for mapping electron and photon beam induced microscopic changes in SiNx during nanopore fabrication. *Nanotechnology* **2020**, *31*, 395202.
- (46) Logan, S. The origin and status of the Arrhenius equation. *Journal of Chemical Education* **1982**, *59* (4), 279-281.
- (47) Kimura, M.; Koyama, H. Mechanism of time-dependent oxide breakdown in thin thermally grown SiO 2 films. *Journal of applied physics* **1999**, *85* (11), 7671-7681.
- (48) Wanunu, M.; Sutin, J.; McNally, B.; Chow, A.; Meller, A. DNA translocation governed by interactions with solid-state nanopores. *Biophysical journal* **2008**, *95* (10), 4716-4725.
- (49) Liang, S.; Xiang, F.; Tang, Z.; Nouri, R.; He, X.; Dong, M.; Guan, W. Noise in nanopore sensors: sources, models, reduction, and benchmarking. *Nanotechnology and Precision Engineering* **2020**, *3* (1), 9-17.

# For TOC only

